Partial-wave representation of the strong-field approximation

Birger Böning [1,2,*] and Stephan Fritzsche [1,2,3]
[1]*Helmholtz-Institut Jena, D-07743 Jena, Germany*
[2]*GSI Helmholtzzentrum für Schwerionenforschung GmbH, D-64291 Darmstadt, Germany*
[3]*Theoretisch-Physikalisches Institut, Friedrich-Schiller-Universität Jena, D-07743 Jena, Germany*

(Received 24 July 2020; accepted 27 October 2020; published 10 November 2020)

The strong-field approximation (SFA) has been widely applied to model ionization processes in short and intense laser pulses. Several approaches have been suggested in order to overcome certain limitations of the original SFA formulation with regard to the representation of the initial bound and final continuum states of the emitted electron as well as a suitable description of the driving laser pulse. We here present a reformulation of the SFA in terms of partial waves and spherical tensor operators that supports a quite simple implementation and the comparison of different treatments of the active (photo)electron and the laser pulses. In particular, this reformulation helps to adapt the SFA to experimental setups, and it paves the way to extend the strong-field theory toward the study of nondipole contributions in light-atom interactions as well as of many-particle correlations in strong-field ionization processes. A series of detailed computations have been carried out in order to confirm the validity of the reformulation and to show how the representation of the bound and continuum states affects the predicted above-threshold ionization spectra and related observables.

DOI: 10.1103/PhysRevA.102.053108

I. INTRODUCTION

In recent decades, strong-field physics has attracted much interest and helped us to understand, probe, and control various *nonlinear* processes in the interaction of light with atoms and molecules. Indeed, much of its success can be attributed to today's ability to precisely tailor the temporal shape and duration of ultrashort laser pulses as well as the development of theoretical methods that account for the nonperturbative interaction with matter. Despite these successes, however, many of the methods in strong-field physics still rely on a simplified treatment of the (atomic) targets and electronic motion in excitation and ionization processes.

Of course, any reliable strong-field theory of processes such as above-threhold ionization (ATI, [1,2]), high-order harmonic generation (HHG, [3,4]), and nonsequential double ionization [5] is based on the time-dependent Schrödinger equation. While a direct numerical integration of this equation often leads to accurate predictions [6], such numerical solutions quickly become infeasible if the motion of one (active) electron is studied in three *plus* spin dimensions or if several electrons are involved in the interaction. Therefore, a number of analytical methods have been developed in order to provide a deeper insight into the underlying dynamics and to explain the various processes mentioned above. In particular, the strong-field approximation (SFA, [7–9]) is nowadays widely applied to model ATI and HHG spectra [10,11].

The original formulation of the SFA, however, has several limitations that hamper its application to modern experimental setups. For example, it neglects the influence of the atomic potential upon the dynamics of the emitted electron(s) and describes their motion simply in terms of (so-called) Volkov continuum states. Moreover, the initial bound state of the electron is usually described in single-active electron approximation or, even simpler, by the ground state of a hydrogenic atom [12,13], quite in contrast to the targets often used in experiments [1,2,14]. Both of these simplifications omit large parts of the electronic structure and dynamics. Recent studies have therefore incorporated the Coulomb potential of the photoion into the representation of the continuum states [15–18] or included even more realistic ionic potentials [19]. In addition, the coupling of the ground and continuum states to other bound states has been accounted for in an SFA-based study of HHG [20] and the dependence of ATI spectra on the initial state and the temporal shape of the driving laser pulse has been considered [21–24]. In practice, however, most of these recent *extensions* of the SFA have been explored separately and with little attempt to combine them into a single framework. This makes it difficult to compare these approaches and to see how they affect the predicted spectra and behavior of atoms in different strong-field processes.

In this work, we therefore reformulate the SFA for the description of ATI in terms of partial waves of the emitted electron and spherical tensor operators. This reformulation facilitates not only the comparison of different treatments of the active (photo)electron and laser pulses but will also help to adapt the SFA to novel experimental setups. Although we shall restrict ourselves to the reformulation of the *direct* SFA transition amplitude, such a partial-wave expansion supports a straigthforward *improvement* in the representation of the initial bound state and the (Volkov) continuum as well as in the description of the driving laser pulses. A series of detailed computations have been carried out in order to confirm the

*b.n.boening@gsi.de

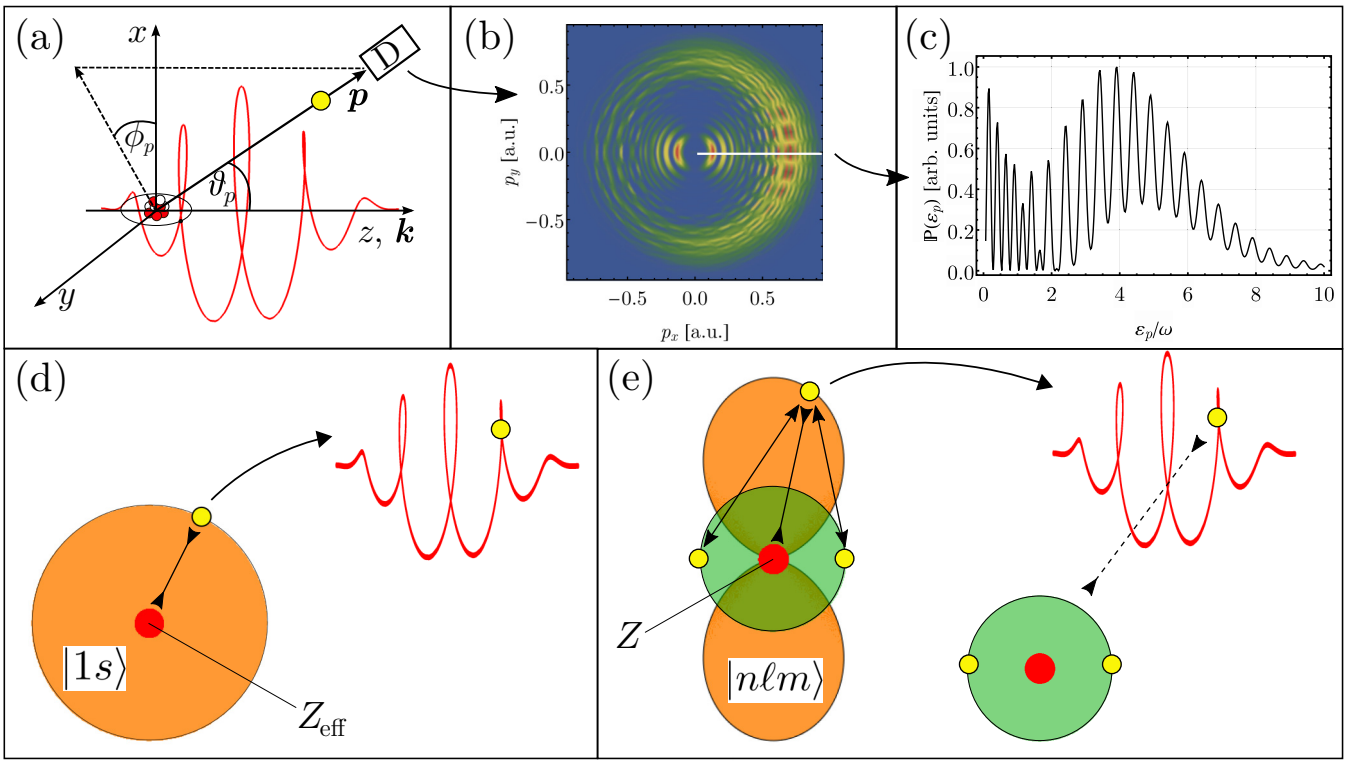

FIG. 1. Overview of ATI and the SFA. (a) Geometry of an ATI experiment: An atom is irradiated by a strong laser pulse (red) that propagates along the z axis and is polarized within the x-y plane. After its interaction with the laser pulse, a photoelectron is emitted with momentum $\boldsymbol{p} = (p, \vartheta_p, \varphi_p)$ in spherical coordinates and measured at the detector D. (b) Typical PMD in the polarization plane ($\vartheta_p = \pi/2$, $p_z = 0$) as recorded by the detector. (c) Photoelectron energy spectra as obtained along the white line in panel (b), i.e., if the azimuthal angle is fixed ($\varphi_p = 0$, $p_y = 0$). This spectrum exhibits the typical ATI peaks. (d) Outline of the usual assumptions that are made in the SFA: The active electron is bound in a hydrogen-like $1s$ initial state by a nucleus with effective charge $Z_{\rm eff}$. The laser pulse excites the active electron into the continuum where it propagates in the electric field of the laser pulse. (e) In a more realistic description of the ionization process, the active electron is bound in the state $|nlm\rangle$ in an atomic (mean-field) potential as caused by the nucleus and the other bound electrons. After the interaction, the electron is in a continuum (state) that is dressed by the laser field *and* the field of the residual ion.

validity of this reformulation and to demonstrate how different representations of the bound and continuum states affect the predicted ATI spectra and related observables. Moreover, since our formulation can be readily coupled to atomic structure calculations, it will pave the way to extend the strong-field theory toward studies of nondipole contributions in light-atom interactions, the treatment of initially excited levels, the rescattering of the electrons at the target, and/or many-particle correlations in strong-field ionization processes.

This paper is structured as follows. In Sec. II, we introduce the theoretical description of ATI within the SFA, before turning to the expansion in terms of partial waves and spherical tensors in Sec. III. To this end, we write the initial and continuum states of the photoelectron in a general form and consider the vector potential of the driving laser pulse in a spherical basis. In Sec. IV, we use our analytical result in order to obtain specific results. In particular, we compare with the standard formulation of the SFA and investigate different laser pulse shapes. Furthermore, we show that the continuum can be easily exchanged in our formulation and perform specific calculations including the Coulomb potential, before we briefly discuss the dependence on the initial bound state and the use of a short-range potential. Finally, we give our conclusions and an outlook for future work in Sec. V.

Atomic units ($m_e = e = \hbar = 4\pi\varepsilon_0 = 1$) are used throughout the paper unless stated otherwise.

II. THEORETICAL FRAMEWORK

A. Overview

Here, we shall reformulate the theoretical description of ATI of an atomic gas target in terms of partial waves and spherical operators. A typical geometry of an ATI experiment is shown in Fig. 1(a), where an atom is irradiated by a strong laser pulse that propagates, for instance, along the z axis and is polarized within the x-y plane. Following the interaction of the pulse with an atom from the target, a photoelectron is emitted and measured at the detector with momentum $\boldsymbol{p} = (p, \vartheta_p, \varphi_p)$, written in spherical coordinates. The photoelectron momentum distribution (PMD) is usually measured in the polarization plane ($\vartheta_p = \pi/2$, $p_z = 0$) as a function of p_x and p_y [cf. Fig. 1(b)]. Then, the typical ATI peaks become visible if the azimuthal angle φ_p is fixed and the energy spectrum of the photoelectrons is measured along a line in the p_x-p_y plane, as indicated in Fig. 1(c). Because of the interaction with the strong laser field, the photoelectron can absorb more photons than needed in order to overcome the ionization threshold,

and this leads to the well-known ATI peaks that are spaced by (fractions of) the photon energy.

In order to compute these PMDs and energy spectra, one often assumes that only one electron is active (*single active electron approximation*) and initially bound in a hydrogenic $1s$ state, while all other electrons are neglected or give rise to an atomic *mean-field* potential. In this picture, the electron undergoes a transition into the laser-dressed continuum due to its interaction with the laser pulse; cf. Fig. 1(d). Obviously, both the correct representation of the initial state of the atoms *and* the influence of the electrostatic potential of the photoion upon the continuum remains neglected in the standard SFA. A more realistic description of this ATI process should therefore at least account for the (effective) interaction of the active electron in its initial state $|nlm\rangle$ with the other bound electrons as well as the potential of the residual ion that acts upon the outgoing photoelectron, in addition to the laser field [cf. Fig. 1(e)].

Below, we first briefly outline the general assumptions and derivation of the SFA for its application to ATI, before we shall reformulate this approximation in terms of partial waves and spherical tensors. This reformulation enables us more readily to account for and to switch between the various assumptions described in the previous paragraph. In particular, we shall focus here upon realistic (single-electron) initial states and the improved representation of the continuum, while a many-electron treatment of the target atoms in the SFA will be considered in forthcoming work.

B. Strong-field approximation

The SFA provides an analytical formalism to compute the energy- and angle-differential photoionization probability for the ATI of atoms in strong laser fields [12],

$$\mathbb{P}(\boldsymbol{p}) = p|\mathbb{T}(\boldsymbol{p})|^2, \tag{1}$$

in terms of a transition amplitude $\mathbb{T}(\boldsymbol{p})$ and where $\boldsymbol{p}$ refers to the photoelectron momentum as measured at the detector. In this formalism, moreover, a single active electron is assumed that is initially bound in a state $|\Psi_i(t)\rangle$ and, after its interaction with the laser field, is found in a final state $|\Psi_{\boldsymbol{p}}(t)\rangle$ with asymptotic momentum $\boldsymbol{p}$ at the detector. The dynamics of the electron follows the Schrödinger equation

$$i\frac{\partial}{\partial t}|\Psi(t)\rangle = \hat{H}\,|\Psi(t)\rangle\,, \tag{2}$$

with the Hamiltonian given by

$$\hat{H} = \frac{\hat{\boldsymbol{p}}^2}{2} + V_{\rm le}(\boldsymbol{r},t) + V(\boldsymbol{r}). \tag{3}$$

Here, $V_{\rm le}(\boldsymbol{r},t) = \boldsymbol{A}(\boldsymbol{r},t)\hat{\boldsymbol{p}} + \boldsymbol{A}^2(\boldsymbol{r},t)/2 - \phi(\boldsymbol{r},t)$ is the laser-electron interaction potential with the electromagnetic scalar and vector potentials $\phi(\boldsymbol{r},t)$ and $\boldsymbol{A}(\boldsymbol{r},t)$, respectively. Furthermore, $V(\boldsymbol{r})$ denotes the atomic binding potential, which is often simply approximated by the Coulomb potential of the photoion.

In general, the transition amplitude can be written as

$$\mathbb{T}(\boldsymbol{p}) = \lim_{t\to\infty,t'\to-\infty} \langle\Psi_{\boldsymbol{p}}(t)|\hat{U}(t,t')|\Psi_i(t')\rangle\,,$$

where $\hat{U}(t,t')$ is the exact time evolution operator corresponding to the Hamiltonian (3). In order to simplify this transition amplitude, the SFA makes the following assumptions:

(1) The influence of the laser field on the bound states is negligible; i.e., the initial state $|\Psi_i\rangle$ is just taken as a bound state of the atomic Hamiltonian $\hat{H}_A = \hat{\boldsymbol{p}}^2/2 + \hat{V}(\boldsymbol{r})$.

(2) The final state, measured at the detector, is a plane wave, i.e., $|\Psi_{\boldsymbol{p}}\rangle = |\boldsymbol{p}\rangle$.

(3) The influence of the atomic potential $V(\boldsymbol{r})$ upon the electronic motion in the continuum is negligible in the time evolution operator, i.e., $\hat{U}(t,t') \approx \hat{U}_{\rm le}(t,t')$ with the time evolution operator $\hat{U}_{\rm le}(t,t')$ corresponding to the Hamiltonian $\hat{H}_{\rm le} = \hat{\boldsymbol{p}}^2/2 + \hat{V}_{\rm le}(\boldsymbol{r},t)$.

With these assumptions in mind, the transition amplitude $\mathbb{T}(\boldsymbol{p})$ takes the form [12]

$$\mathbb{T}(\boldsymbol{p}) = \mathbb{T}_0(\boldsymbol{p}) + \mathbb{T}_1(\boldsymbol{p}), \tag{4a}$$

$$\mathbb{T}_0(\boldsymbol{p}) = -i\int_{-\infty}^{\infty} d\tau\ \langle\chi_{\boldsymbol{p}}(\tau)|V_{\rm le}(\boldsymbol{r},t)|\Psi_i(\tau)\rangle\,, \tag{4b}$$

$$\mathbb{T}_1(\boldsymbol{p}) = (-i)^2\int_{-\infty}^{\infty} d\tau \int_{\tau}^{\infty} d\tau'\ \langle\chi_{\boldsymbol{p}}(\tau')|V(\boldsymbol{r})\hat{U}_{\rm le}(\tau',\tau)V_{\rm le}(\boldsymbol{r},\tau)|\Psi_i(\tau)\rangle\,, \tag{4c}$$

where $|\chi_{\boldsymbol{p}}\rangle$ denotes a continuum state of the photoelectron in the laser field. The two amplitudes $\mathbb{T}_0(\boldsymbol{p})$ and $\mathbb{T}_1(\boldsymbol{p})$ can be readily interpreted in terms of photoelectrons that directly propagate to the detector and are rescattered at the photoion, respectively, and they are often briefly referred to as direct and rescattering amplitudes. Up to this point, no assumptions have been made about the form of the atomic potential $V(\boldsymbol{r})$ and how the potentials $\phi(\boldsymbol{r},t)$ and $\boldsymbol{A}(\boldsymbol{r},t)$ of the driving laser field affect the continuum states $|\chi_{\boldsymbol{p}}\rangle$.

Further simplifications are necessary and typically applied in order to evaluate the transition amplitude (4a) for specific physical scenarios. First, the laser field is usually considered only in dipole approximation, $\boldsymbol{A}(\boldsymbol{r},t) \approx \boldsymbol{A}(t)$, and hence, both the magnetic field and the spatial dependence of the electric field are neglected. This simplification, in particular, allows for a straightforward solution for the continuum states and we will make use of it for the remainder of this work. Second, the initial state $|\Psi_i(t)\rangle$ is assumed to be a hydrogen-like initial state (often $|1s\rangle$). Our reformulation of the (direct) SFA transition amplitude (4b) in terms of partial waves and spherical tensors in the next section will enable us to account for a more appropriate description of the initial state as well as to readily replace the continuum states and the shape (envelope) of the driving laser pulse as suitable for numerical implementations

and, likely, even for the ATI of few- and multielectron atoms in the future.

III. REFORMULATION OF SFA BY MEANS OF PARTIAL WAVES AND SPHERICAL TENSORS

To compute the transition amplitude (4), we need to specify the initial state of the active electron, the vector potential of the driving laser pulse, and the continuum state for the outgoing electron wave. Typically, one chooses them appropriate to the given setup of an experiment and according to a number of practical considerations in order to keep the computation of the transition amplitude (4) feasible. Several of the *standard* approximations that are often used right from the beginning in the simplification of the transition amplitude have been mentioned above. In contrast, here we rewrite this amplitude without further approximations but by applying a partial-wave representation of the initial- and final-state wave functions (of the active electron) and spherical tensor operators to separate the *directional* dependence of the amplitude from the physical interaction. In particular, we represent these single-electron states and the vector potential within a spherical basis, in which the (integration over) radial and spherical coordinates can be readily separated. Overviews of spherical tensors and the spherical basis formalism that we use below can be found, for example, in Refs. [25,26].

A. Initial state

Initially, the active electron is taken to be in a (nonrelativistic) eigenstate of the atomic Hamiltonian,

$$|\Psi_i(t)\rangle = e^{-i\varepsilon_i t}\,|\psi_i\rangle = e^{-i\varepsilon_i t}\,|n\ell m\rangle \otimes |\chi_{s,m_s}\rangle\,, \tag{5}$$

characterized by the principal and orbital angular momentum quantum numbers n, ℓ, and m, respectively, as well as the projection m_s of the electron spin $s = 1/2$. Here, the eigenvalue ε_i denotes the binding energy (or ionization potential $I_p = -\varepsilon_i$) of the electron and, in position space, the eigenstates are usually written

$$\begin{aligned}\Psi_i(\boldsymbol{r},t) &= \psi_i(\boldsymbol{r})e^{-i\varepsilon_i t}\,\chi_{s,m_s} \\ &= \frac{P_{n\ell}(r)}{r} Y_{\ell m}(\vartheta,\varphi)e^{-i\varepsilon_i t}\,\chi_{s,m_s}\end{aligned} \tag{6}$$

in terms of the radial wave function $P_{n\ell}(r)$ and the spherical harmonics $Y_{\ell m}(\vartheta,\varphi)$.

B. Continuum states

If the photoelectron is excited into the continuum, it must still obey the full Schrödinger equation (2) with the Hamiltonian $\hat{H}$ that contains both the atomic and the laser-electron interaction potentials. If, as usual in SFA, the atomic potential is neglected for the motion of the photoelectron in the continuum, the continuum states are just given by the (plane-wave) *Volkov states*, although experiments suggest including the atomic binding potential into the representation of the continuum states. For a pure Coulomb potential, one then obtains *Coulomb-Volkov states*, while (so-called) *atom-Volkov states* may refer to a more realistic atomic potential. We shall describe these different representations of the continuum in the following paragraphs. In general, for any central-field potential, we can expand the continuum states into spherical waves,

$$\begin{aligned}|\chi_{\boldsymbol{p}}(t)\rangle = &\sqrt{\frac{2}{\pi}}e^{-iS_V(t)} \\ &\times \sum_{\ell_p=0}^{\infty}\sum_{m_p=-\ell_p}^{\ell_p} Y^*_{\ell_p m_p}(\vartheta_p,\varphi_p)\,|\varepsilon_p\ell_p m_p\rangle\,,\end{aligned} \tag{7}$$

where we use spherical coordinates, $\boldsymbol{p} = (p,\vartheta_p,\varphi_p)$, to express the momentum of the photoelectron with energy $\varepsilon_p = p^2/2$ at the detector. Moreover, we introduced the Volkov phase $S_V(t)$ [see Eq. (11) below] as well as the *partial-wave representation* of the angular momentum states $|\varepsilon_p\ell_p m_p\rangle$ with well-defined asymptotic energy,

$$\langle \boldsymbol{r}|\varepsilon_p\ell_p m_p\rangle = i^{\ell_p}\frac{P_{\varepsilon_p\ell_p}(r)}{r}\,Y_{\ell_p m_p}(\vartheta,\varphi), \tag{8}$$

following the conventions of Ref. [27]. Of course, in such a basis the radial wave function $P_{\varepsilon_p\ell_p}(r)$ will depend on the particular choice of solutions.

Below, we can readily include also the electron spin into the continuum representation by taking the product of Eq. (7) with a spin wave function,

$$|\chi_{\boldsymbol{p},s',m'_s}(t)\rangle = |\chi_{\boldsymbol{p}}(t)\rangle \otimes |\chi_{s',m'_s}\rangle\,.$$

Since the spin of the emitted photoelectron is usually not measured in strong-field atomic experiments, one then has to average over m'_s in the photoionization probability. As seen from the above equations, however, the continuum states are always characterized by the photoelectron momentum $\boldsymbol{p}$ and spin projection, independent of the particular Hamiltonian, while the laser pulse affects the photoelectron only through the Volkov phase $S_V(t)$.

1. Plane-wave Volkov states

The plane-wave Volkov states are known as solutions to the Schrödinger equation (2) for an electron in a purely time-harmonic laser field, i.e., for the approximate Hamiltonian $\hat{H} \approx \hat{H}_{\rm le} = \frac{\hat{\boldsymbol{p}}^2}{2} + V_{\rm le}(\boldsymbol{r},t)$. The laser field is usually described either in length gauge by the laser-electron interaction potential $V_{\rm le}(\boldsymbol{r},t) = -\phi(\boldsymbol{r},t) = -\boldsymbol{d}\cdot\boldsymbol{E}(t)$ together with the dipole operator $\boldsymbol{d} = q\boldsymbol{r} = -\boldsymbol{r}$ and the electric field $\boldsymbol{E}(t)$, *or* in velocity-gauge where

$$V_{\rm le}(\boldsymbol{r},t) = \boldsymbol{A}(t)\cdot\hat{\boldsymbol{p}} + \tfrac{1}{2}\boldsymbol{A}^2(t). \tag{9}$$

In either of these gauges, the Volkov states can be easily constructed from the Schrödinger equation. In velocity gauge, they are explicitly given by

$$\chi_{\boldsymbol{p}}(\boldsymbol{r},t) = \frac{1}{(2\pi)^{3/2}}e^{-iS_V(t)}e^{i\boldsymbol{p}\cdot\boldsymbol{r}}, \tag{10}$$

where we have introduced the Volkov phase

$$S_V(t) = \frac{1}{2}\int^t d\tau\;(\boldsymbol{p}+\boldsymbol{A}(\tau))^2, \tag{11}$$

which is equal to the classical action of the electron moving in the time-dependent laser field.

In velocity gauge, we can make use of the spherical-wave expansion [27],

$$\frac{e^{i\boldsymbol{p}\cdot\boldsymbol{r}}}{4\pi} = \sum_{\ell_p=0}^{\infty}\sum_{m_p=-\ell_p}^{\ell_p} i^{\ell_p} j_{\ell_p}(pr) Y^*_{\ell_p m_p}(\vartheta_p,\varphi_p) Y_{\ell_p m_p}(\vartheta,\varphi), \quad (12)$$

in order to rewrite the Volkov states (10) and where $j_{\ell_p}(x)$ are spherical Bessel functions. If we compare the result with Eqs. (7) and (8), we can immediately read off the radial wave function,

$$P_{\varepsilon_p\ell_p}(r) = r\, j_{\ell_p}(pr), \quad p=\sqrt{2\varepsilon_p}. \quad (13)$$

In principle, the expansion (12) may also be applied to the Volkov states in length gauge [19]. However, the additional factor $e^{i\boldsymbol{A}(t)\cdot\boldsymbol{r}}$ then leads to terms of the form $j_\ell(A(t)r)$ in the final expression that complicate the subsequent analysis. From here on, we will therefore focus on the SFA in velocity gauge and leave the reformulation in length gauge as a future task. One should, however, always keep in mind that the length-gauge SFA yields more accurate results than the velocity-gauge formulation, especially for initial p states [28].

2. Coulomb-Volkov states

If the potential of the photoion is not neglected right from the beginning, it can be approximated in the first instance by a Coulomb potential. That is, we can construct continuum solutions to the Schrödinger equation (2) with the Hamiltonian (3) and a Coulomb binding potential $V(\boldsymbol{r}) = V_C(r) = -Z/r$ of the residual ion with charge Z. These solutions are often *approximated* by the Coulomb-Volkov states that are Coulomb waves $|\phi_{\boldsymbol{p}}^{(C)}\rangle$ multiplied by the Volkov phase factor from above [18,29],

$$|\chi_{\boldsymbol{p}}(t)\rangle = \frac{1}{(2\pi)^{3/2}} e^{-iS_V(t)} \left|\phi_{\boldsymbol{p}}^{(C)}\right\rangle, \quad (14)$$

and where the Volkov phase is again given by Eq. (11). In position space, the outgoing Coulomb waves asymptotically become plane waves, $\phi_{\boldsymbol{p}}^{(C)}(\boldsymbol{r}) \to e^{i\boldsymbol{p}\boldsymbol{r}}$ for $\boldsymbol{p}\boldsymbol{r}\to+\infty$, and have the explicit form

$$\phi_{\boldsymbol{p}}^{(C)}(\boldsymbol{r}) = e^{\frac{\pi}{2}\eta_p}\Gamma(1+i\eta_p) e^{i\boldsymbol{p}\cdot\boldsymbol{r}} {}_1F_1(-i\eta_p;1;-i(pr+\boldsymbol{p}\boldsymbol{r})), \quad (15)$$

where $\eta_p = -Z/p$, $\Gamma(x)$ is the Γ function, and ${}_1F_1(a;b;c)$ is the confluent hypergeometric function [30]. The outgoing Coulomb waves can be rewritten in a partial-wave expansion, analogous to Eq. (12), as [26]

$$\phi_{\boldsymbol{p}}^{(C)}(\boldsymbol{r}) = 4\pi \sum_{\ell_p=0}^{\infty}\sum_{m_p=-\ell_p}^{\ell_p} i^{\ell_p} \frac{w_{\ell_p}(\eta_p,pr)}{r} Y^*_{\ell_p m_p}(\vartheta_p,\varphi_p) Y_{\ell_p m_p}(\vartheta,\varphi), \quad (16)$$

and we explicitly state the functions $w_{\ell_p}(\eta_p,pr)$ in Appendix A. From a comparison with Eqs. (7) and (8), we find that the radial wave function is given by

$$P_{\varepsilon_p\ell_p}(r) = w_{\ell_p}(\eta_p,pr). \quad (17)$$

3. Atom-Volkov states

While the Coulomb potential above accounts for the long-range influence of the photoion, an even more realistic description is obtained for the continuum states, if a short-range potential $V_{SR}(r)$ is added to the Coulomb potential $V_C(r) = -Z/r$ in the Hamiltonian (3). Then, the full potential may be written, for example, as [19]

$$\begin{aligned} V(r) &= V_C(r) + V_{SR}(r), \\ &= -\frac{Z + a_1 e^{-a_2 r} + a_3 e^{-a_4 r} + a_5 e^{-a_6 r}}{r}, \end{aligned} \quad (18)$$

where the coefficients $a_1 - a_5$ depend on the target atom in question [31,32].

Analogous to the Coulomb-Volkov states, the continuum states $|\chi_{\boldsymbol{p}}(t)\rangle$ in the potential (18) and the laser field can be constructed from distorted scattering states $|\phi_{\boldsymbol{p}}^{(A)}\rangle$ that are solutions to the stationary Schrödinger equation with the Hamiltonian $\hat{H} = \frac{\hat{\boldsymbol{p}}^2}{2} + V(r)$: They are approximated again by multiplying $|\phi_{\boldsymbol{p}}^{(A)}\rangle$ with the Volkov phase factor with the Volkov phase (11),

$$|\chi_{\boldsymbol{p}}(t)\rangle = \frac{1}{(2\pi)^{3/2}} e^{-iS_V(t)} \left|\phi_{\boldsymbol{p}}^{(A)}\right\rangle,$$

and can again explicitly be written in the form of Eqs. (7) and (8) with the radial wave function [19]

$$P_{\varepsilon_p\ell_p}(r) = \tilde{P}_{\varepsilon_p\ell_p}(r) e^{i(\sigma_{\ell_p}+\delta_{\ell_p})}. \quad (19)$$

In these radial functions, a phase shift δ_{ℓ_p} arises due to the short-range potential in addition to the Coulomb phase shift σ_{ℓ_p}; cf. Appendix A. It can be extracted from the asymptotic behavior of the radial wave function for large r; cf. Ref. [33]. The (yet) unknown functions $\tilde{P}_{\varepsilon_p\ell_p}(r)$ can be determined numerically as solutions of the radial Schrödinger equation in the potential (18) form above,

$$\left[-\frac{1}{2}\frac{1}{r^2}\frac{\partial}{\partial r}\left(r^2\frac{\partial}{\partial r}\right) + \frac{\ell_p(\ell_p+1)}{2r^2} + V(r) - \varepsilon_p\right]\frac{\tilde{P}_{\varepsilon_p\ell_p}(r)}{r} = 0.$$

This ansatz for the photoelectron continuum states has been called *atom-Volkov ansatz* in Ref. [19] and we shall refer to the associated continuum states $|\chi_{\boldsymbol{p}}(t)\rangle$ as *atom-Volkov states* below. Instead of using Eq. (18), of course, an effective potential $V(r)$ of the residual ion can be readily determined also from atomic-structure calculations and then leads to modified radial wave functions $\tilde{P}_{\varepsilon_p\ell_p}(r)$ in the representation of the *atom-Volkov states*.

C. Vector potential

Both the transition amplitude (4) and the continuum states discussed above contain the vector and scalar potentials of the (plane-wave) driving laser pulse. Since we restrict ourselves to the dipole approximation and the velocity gauge, the scalar potential vanishes identically and the electric field of the pulse is simply defined by a purely time-dependent vector potential $\boldsymbol{A}(t)$. In particular, let us start here from the complex-valued vector potential of an elliptically polarized laser pulse of the form

$$\boldsymbol{A}_c(t) = A_0\, \boldsymbol{u}\; f(t)\; e^{-i(\omega t + \phi_{\rm CEP})}, \tag{20}$$

with the (real-valued) amplitude A_0, the pulse envelope $f(t)$, the frequency ω, the carrier-envelope phase $\phi_{\rm CEP}$, and the (complex) polarization unit vector $\boldsymbol{u}$.

From a physics viewpoint, since both the laser-electron interaction operator $V_{\rm le}(\boldsymbol{r}, t)$ and the Volkov phase (11) contain terms nonlinear in $\boldsymbol{A}(t)$ and the physical electric field is real, we shall consider only the real part of Eq. (20),

$$\boldsymbol{A}(t) = {\rm Re}\{\boldsymbol{A}_c(t)\} = \tfrac{1}{2}[\boldsymbol{A}_c(t) + \boldsymbol{A}_c^*(t)]. \tag{21}$$

If the laser pulse propagates along the z axis [cf. Fig. 1(a)], the polarization unit vector lies in the x-y plane and has the explicit form

$$\boldsymbol{u} = \frac{1}{\sqrt{1+\varepsilon^2}}(\boldsymbol{e}_x + i\lambda\varepsilon\boldsymbol{e}_y),$$

where $\lambda = \pm 1$ and $0 \leqslant \varepsilon \leqslant 1$ refer to the helicity and ellipticity of the pulse, respectively. To reformulate the SFA transition amplitude by means of partial waves and spherical tensor operators, we first write the polarization unit vector as a *spherical vector*,

$$\boldsymbol{u} = \sum_{q=0,\pm 1} u_q \boldsymbol{e}_q, \tag{22}$$

where the (covariant) spherical basis vectors $\boldsymbol{e}_+$, $\boldsymbol{e}_-$, and $\boldsymbol{e}_0$ are given in terms of Cartesian basis vectors by [34]

$$\boldsymbol{e}_\pm = \mp\frac{\boldsymbol{e}_x \pm i\boldsymbol{e}_y}{\sqrt{2}}, \quad \boldsymbol{e}_0 = \boldsymbol{e}_z.$$

Similarly, the spherical components $u_q = \langle \boldsymbol{u}, \boldsymbol{e}_q \rangle$ of the polarization unit vector are related to its Cartesian components by

$$u_\pm = \frac{\mp u_x + i u_y}{\sqrt{2}}, \quad u_0 = u_z,$$

or, explicitly, by

$$u_+ = -\frac{1}{\sqrt{2(1+\varepsilon^2)}}(1+\lambda\varepsilon),$$

$$u_- = \frac{1}{\sqrt{2(1+\varepsilon^2)}}(1-\lambda\varepsilon),$$

$$u_0 = 0.$$

In particular, for a left-circularly polarized pulse ($\lambda = +1$, $\varepsilon = 1$) we find $u_+ = -1$ and $u_- = 0$, while for a right-circularly polarized pulse ($\lambda = -1$, $\varepsilon = 1$) we find $u_+ = 0$ and $u_- = 1$. For linear polarization ($\varepsilon = 0$), these equations reduce to $u_+ = -u_- = -1/\sqrt{2}$.

Below, we will consider different temporal shapes of the laser pulse, as defined by the envelope $f(t)$. For the sake of simplicity, one often assumes a continuous laser beam with $f(t) = 1$ in order to approximate long pulses with many optical cycles. For short pulses, in contrast, a rectangular envelope may be utilized, $f(t) = 1$ for $0 \leqslant t \leqslant T_p$ and $f(t) = 0$ otherwise, if the pulse has duration $T_p = 2\pi n_p/\omega$ and comprises an (integer) number n_p of optical cycles. An experimentally more realistic pulse is given by a sine-squared pulse with envelope $f(t) = \sin^2(\omega t/2n_p)$ for $0 \leqslant t \leqslant T_p = 2\pi n_p/\omega$ and $f(t) = 0$ otherwise. Such pulses are often used within the SFA, since they allow an analytical evaluation of the Volkov phase in terms of elementary functions [12]. In addition, Gaussian pulses with the envelope $f(t) = e^{-4\ln(2)(t/T_p)^2}$ may be considered and for which the pulse duration T_p is defined as the full-width at half maximum of the envelope. For these four pulse shapes, we state the Volkov phase (11) for circular polarization explicitly in Appendix B.

In general, a driving laser pulse with given envelope $f(t)$ is completely specified by its amplitude A_0, frequency ω, ellipticity ε, helicity λ, pulse duration T_p as well as its carrier-envelope phase $\phi_{\rm CEP}$. The (maximum) intensity of the pulse can be easily computed by $I = A_0^2\omega_0^2 c/8\pi$ from the amplitude A_0.

D. Direct transition amplitude

With the various definitions above for the initial and continuum states of the photoelectron as well as the laser pulse, we can now rewrite the direct SFA transition amplitude (4b) in terms of partial waves and spherical tensors. Making use of the vector potential (21), the laser-electron interaction potential (9) takes the form

$$V_{\rm le}(\boldsymbol{r}, t) = -\frac{i}{2}\boldsymbol{A}_c(t)\cdot\boldsymbol{\nabla} - \frac{i}{2}\boldsymbol{A}_c^*(t)\cdot\boldsymbol{\nabla} + \frac{1}{8}[\boldsymbol{A}_c(t) + \boldsymbol{A}_c^*(t)]^2$$

and can be directly inserted into the matrix element in the amplitude (4b), together with the initial state (5) as well as the spin part $|\chi_{s',m_s'}\rangle$ and the general form of the continuum states (7),

$$\langle \chi_{\boldsymbol{p},s',m_s'}(\tau)|V_{\rm le}(\boldsymbol{r},\tau)|\Psi_i(\tau)\rangle = \sqrt{\frac{2}{\pi}} e^{iS_V(\tau)} e^{-i\varepsilon_i\tau}\, \langle \chi_{s',m_s'}|\chi_{s,m_s}\rangle \sum_{\ell_p=0}^{\infty}\sum_{m_p=-\ell_p}^{\ell_p} Y_{\ell_p m_p}(\vartheta_p,\varphi_p)\Big[A_0\, f(\tau)\, e^{-i(\omega\tau+\phi_{\rm CEP})}\, \langle \varepsilon_p \ell_p m_p|\boldsymbol{u}\cdot\hat{\boldsymbol{p}}|n\ell m\rangle$$

$$+\, A_0\, f(\tau)\, e^{i(\omega\tau+\phi_{\rm CEP})}\, \langle \varepsilon_p \ell_p m_p|\boldsymbol{u}^*\cdot\hat{\boldsymbol{p}}|n\ell m\rangle + \frac{1}{2}A^2(\tau)\, \langle \varepsilon_p \ell_p m_p|n\ell m\rangle\Big].$$

The scalar products in the electron-photon interaction matrix elements (second and third term) can be explicitly evaluated using the polarization vector (22) in the spherical basis,

$$\boldsymbol{u}\cdot\hat{\boldsymbol{p}} = \sum_{q=0,\pm1} (-1)^q u_q \hat{p}_{-q},$$
$$\boldsymbol{u}^*\cdot\hat{\boldsymbol{p}} = \sum_{q=0,\pm1} u_q^* p_q,$$

where we use the spherical components $\hat{p}_q$ of the momentum operator analogous to Eq. (22). The matrix elements of $\boldsymbol{u}\cdot\hat{\boldsymbol{p}}$ then become

$$\langle \varepsilon_p \ell_p m_p | \boldsymbol{u}\cdot\hat{\boldsymbol{p}} | n\ell m\rangle = \sum_{q=0,\pm1} (-1)^q u_q \, \langle \varepsilon_p \ell_p m_p | \hat{p}_{-q} | n\ell m\rangle \,.$$

Moreover, since the momentum operator $\hat{p}$ is a first-rank tensor operator, we can apply the Wigner-Eckart theorem in the form [34]

$$\langle jm | T_q^{(k)} | j'm'\rangle = \frac{(-1)^{2k}}{\sqrt{2j+1}} \langle j'm', kq | jm\rangle \, \langle j \| T^{(k)} \| j'\rangle \,,$$

for any tensor operator $T^{(k)}$ of rank k and with spherical components $T_q^{(k)}$, in order to express the matrix elements as

$$\langle \varepsilon_p \ell_p m_p | \boldsymbol{u}\cdot\hat{\boldsymbol{p}} | n\ell m\rangle = \frac{1}{\sqrt{2\ell_p+1}} \sum_{q=0,\pm1} (-1)^q u_q \times \langle \ell m, 1(-q) | \ell_p m_p\rangle \, \langle \varepsilon_p \ell_p \| \hat{\boldsymbol{p}} \| n\ell\rangle \,,$$

in terms of the reduced matrix elements $\langle \varepsilon_p \ell_p \| \hat{\boldsymbol{p}} \| n\ell\rangle$ of $\hat{p}$ as well as the Clebsch-Gordan coefficients $\langle j_1 m_1, j_1 m_2 | jm\rangle$. These Clebsch-Gordan coefficients capture all the directional dependence of the laser-electron interaction. The reduced matrix elements of the momentum operator are derived and shown explicitly in Appendix C. Similar expressions follow directly also for the matrix elements of $\boldsymbol{u}\cdot\hat{\boldsymbol{p}}$.

With this standard decomposition of (almost) all matrix elements in atomic-structure theory and by using the elliptically polarized laser pulse (20), the direct transition amplitude (4b) can now be written

$$\begin{aligned}
\mathbb{T}_0(\boldsymbol{p}) &= -i\int_{-\infty}^{\infty} d\tau \;\; \langle \chi_{\boldsymbol{p},s',m_s'}(\tau) | V_{\rm le}(\boldsymbol{r},\tau) | \Psi_i(\tau)\rangle \\
&= -i\sqrt{\frac{2}{\pi}} \mathcal{F}_1[\omega; f; \boldsymbol{p}] \, \langle \chi_{s',m_s'} | \chi_{s,m_s}\rangle \left(\sum_{\ell_p=0}^{\infty} \sum_{q=0,\pm1} \frac{(-1)^q \, u_q}{\sqrt{2\ell_p+1}} \, Y_{\ell_p,m-q}(\vartheta_p,\varphi_p) \, \langle \ell m, 1(-q) | \ell_p m-q\rangle \, \langle \varepsilon_p \ell_p \| \hat{\boldsymbol{p}} \| n\ell\rangle \right) \\
&\quad - i\sqrt{\frac{2}{\pi}} \mathcal{F}_1[-\omega; f; \boldsymbol{p}] \, \langle \chi_{s',m_s'} | \chi_{s,m_s}\rangle \left(\sum_{\ell_p=0}^{\infty} \sum_{q=0,\pm1} \frac{u_q^*}{\sqrt{2\ell_p+1}} \, Y_{\ell_p,m+q}(\vartheta_p,\varphi_p) \, \langle \ell m, 1q | \ell_p m+q\rangle \, \langle \varepsilon_p \ell_p \| \hat{\boldsymbol{p}} \| n\ell\rangle \right) \\
&\quad - i\frac{1}{\sqrt{2\pi}} \mathcal{F}_2[f; \boldsymbol{p}] \, \langle \chi_{s',m_s'} | \chi_{s,m_s}\rangle \, Y_{\ell m}(\vartheta_p,\varphi_p) \, \langle \varepsilon_p \ell m | n\ell m\rangle \,. \qquad (23)
\end{aligned}$$

In this expression for the direct transition amplitude, we have also defined the two *pulse-shape integrals*

$$\mathcal{F}_1[\pm\omega; f; \boldsymbol{p}] = A_0 e^{\mp i\phi_{\rm CEP}} \int_{-\infty}^{\infty} d\tau \;\; f(\tau) \, e^{-i(\varepsilon_i \pm \omega)\tau + iS_V(\tau)}, \qquad (24a)$$

$$\mathcal{F}_2[f; \boldsymbol{p}] = \int_{-\infty}^{\infty} d\tau \; \boldsymbol{A}^2(\tau) \, e^{-i\varepsilon_i\tau + iS_V(\tau)}, \qquad (24b)$$

that contain the (full) time dependence of the driving laser pulse in terms of the envelope $f(t)$ and only parametrically depend on the photoelectron momentum $\boldsymbol{p}$ at the detector. In addition, we used the identity

$$\langle \ell m, 1(\pm q) | \ell_p m_p\rangle = \langle \ell m, 1(\pm q) | \ell_p (m\pm q)\rangle \, \delta_{m_p, m\pm q}$$

to reduce the summation over the magnetic quantum number m_p in the representation of the continuum.

In the dipole approximation, the summation over the final-state angular momentum ℓ_p could by further reduced by using the symmetry properties of the Clebsch-Gordan coefficients and of the reduced matrix elements of the momentum operator. We will not make this step here since it does not apply if nondipole contributions are to be considered in some forthcoming work [35]. Instead, this reduction can be easily made in any implementation by just using the known selection rules of the Clebsch-Gordan coefficients.

The scalar product $\langle \varepsilon_p \ell m | n\ell m\rangle$ in the last term of Eq. (23) can, due to the orthogonality of spherical harmonics, be written as

$$\langle \varepsilon_p \ell m | n\ell m\rangle = (-i)^\ell \int dr \; P^*_{\varepsilon_p \ell}(r) \, P_{n\ell}(r).$$

Therefore, this scalar product must vanish if $|n\ell m\rangle$ and $|\varepsilon_p \ell_p m_p\rangle$ are eigenstates of the same Hamiltonian, i.e., for initial and continuum states that correspond to the same Hamiltonian. In this particular situation, the $\boldsymbol{A}^2(\tau)$ term will not contribute within the dipole approximation, although it is likely retained in general due to the spatial structure of the light field. For plane-wave Volkov or Coulomb-Volkov states, however, the last term in the expansion (23) needs to be taken into account since $P_{n\ell}(r)$ and $P_{\varepsilon_p \ell}(r)$ are not eigenstates of the same Hamiltonian in that case.

Since, within the nonrelativistic theory, the electron-photon interaction is spin independent, the scalar products of spin states $\langle \chi_{s',m_s'} | \chi_{s,m_s} \rangle \sim \delta_{ss'} \delta_{m_s m_s'}$ do not provide further information and could (as usual) be omitted right from the beginning. We include these spin states here explicitly in Eq. (23) as we wish to generalize the SFA amplitudes toward a relativistic and/or many-electron treatment. In both cases, the electron spin couples to the spatial motion of the electrons and will hence affect the transition amplitudes.

We further note that an experimental target typically consists of unpolarized atoms; that is, the magnetic quantum number m of the initial state is randomly distributed. In order to obtain the corresponding photoionization probability, Eq. (1) needs to be averaged over m,

$$\mathbb{P}(\boldsymbol{p}) = \frac{p}{2\ell+1} \sum_{m=-\ell}^{\ell} \left| \mathbb{T}_0^{(m)}(\boldsymbol{p}) \right|^2, \tag{25}$$

where $\mathbb{T}_0^{(m)}(\boldsymbol{p})$ denotes the transition amplitude for fixed m according to Eq. (23).

Taking the preceding remarks into account, the expansion of the direct ampliude (23) in terms of partial waves and (matrix elements of) spherical tensors is the main *analytical* result of this work. This expansion enables one to readily incorporate and discuss different contributions from the electron-photon interaction and the representation of the active electron without the need to rederive the transition amplitude for every scenario separately. In particular, the initial-state wave function of the active electron is no longer restricted to hydrogenic wave functions but can be easily replaced by any appropriate (radial) function $P_{n\ell}(r)$ in Eq. (6). Furthermore, the representation of the continuum can be replaced by any proper set of (continuum) functions $\{P_{\varepsilon_p \ell_p}(r)\}$ as introduced in Eq. (8). Of course, the particular choices of the initial and continuum state radial wave functions determine the reduced matrix elements of the momentum operator; cf. Eq. (C1) in Appendix C. Finally, the shape of the laser pulse can be modified by including some appropriate pulse envelope $f(t)$ and the associated Volkov phase $S_V(t)$ in Eq. (23).

This rather *modular* form of the transition amplitude also facilitates any (numerical) implementation of the SFA that aims at studying different experimental setups within different approximations. Because of its use of partial waves and spherical tensors, moreover, it may even be coupled to atomic-structure computations and to the question how electronic correlations will affect the strong-field ionization and related processes.

IV. NUMERICAL RESULTS

To demonstrate the versatility of the expansion (23) for the direct SFA transition amplitude, we shall apply it to several scenarios. First, however, we will show its consistency with the standard SFA formulation, i.e., with the direct numerical evaluation of the transition amplitude (4b). We then investigate the dependence of the photoelectron energy spectra on the choice of the pulse envelope for a short driving laser pulse. We also demonstrate that both Coulomb and short-range interactions can be easily incorporated into the continuum by replacing the radial wave functions. Finally, we shall also briefly consider the influence of the initial bound state. All results are presented for left-circularly polarized laser pulses with $\varepsilon = 1$ and $\lambda = +1$.

Below, we either consider the momentum distribution $\mathbb{P}(p_x, p_y, p_z = 0)$ of the emitted photoelectrons in the polarization plane of the driving laser pulse or the photoelectron energy spectrum $\mathbb{P}(\varepsilon_p)$, given by the differential photoionization probability (1) at some fixed polar and azimuthal emission angles $\vartheta_p = \vartheta_p^{(0)}$ and $\varphi_p^{(0)}$,

$$\mathbb{P}(\varepsilon_p) = \mathbb{P}\big(\varepsilon_p, \vartheta_p^{(0)}, \varphi_p^{(0)}\big) \approx p \left| \mathbb{T}_0(\varepsilon_p, \vartheta_p^{(0)}, \varphi_p^{(0)}) \right|^2,$$

and where we approximate the full SFA transition amplitude $\mathbb{T}(\boldsymbol{p})$ by the direct amplitude $\mathbb{T}_0(\boldsymbol{p})$. The photoelectron energy spectrum $\mathbb{P}(\varepsilon_p)$ will also be referred to as *ATI spectrum*.

A. Comparison with standard SFA formulation

We first compare the ATI spectra as obtained from the commonly used form (4b) of the direct SFA transition amplitude and from our reformulation in (23) in terms of partial waves and spherical tensors. We here assume a hydrogen-like $1s$ initial state ($n = 1$, $\ell = 0$, $m = 0$), for which the radial wave function in Eq. (6) is given by

$$P_{10}(r) = 2^{5/2} I_p^{3/2}\, r\, e^{-\sqrt{2I_p} r},$$

with the ionization potential $I_p = -\varepsilon_i = 14\,\mathrm{eV}$ of krypton. Furthermore, we assume that the continuum can be described by the plane-wave Volkov states (10) with the radial wave function (13) and that the laser pulse has a sine-squared envelope (cf. Sec. III C).

With these assumptions in mind, the direct SFA transition amplitude (4b) can be obtained from an analytical evaluation of the matrix element in the time integral (see, for example, Ref. [12]) and by a subsequent numerical integration over t. Alternatively, one can reduce Eq. (23) analytically to

$$\begin{aligned} \mathbb{T}_0(\boldsymbol{p}) = -\frac{i}{\sqrt{2}\pi} \big(& \mathcal{F}_1[\omega; f; \boldsymbol{p}]\, (\boldsymbol{u} \cdot \boldsymbol{e}_p)\, \langle \varepsilon_p 1 \| \hat{\boldsymbol{p}} \| 10 \rangle \\ & + \mathcal{F}_1[-\omega; f; \boldsymbol{p}]\, (\boldsymbol{u}^* \cdot \boldsymbol{e}_p)\, \langle \varepsilon_p 1 \| \hat{\boldsymbol{p}} \| 10 \rangle \\ & + \frac{1}{2} \mathcal{F}_2[f; \boldsymbol{p}]\, \langle \varepsilon_p 00 | 100 \rangle \big), \end{aligned}$$

where $\boldsymbol{e}_p = \boldsymbol{p}/p$, and use this expression in order to compute ATI spectra. In our implementation, however, we solve both the radial integrals in the reduced matrix elements [cf. Eq. (C1) in Appendix C] and the pulse-shape integrals (24) numerically and compute the ATI spectra from the general expression (23). In practice, the computation times are comparable, although slightly longer in our reformulation and for arbitrary initial states and laser polarizations, owing to the necessary summations in Eq. (23).

Figure 2 shows the ATI spectra as obtained for a specific set of parameters from the standard and our reformulation of SFA, respectively. In both spectra, the typical ATI peaks are visible which result from the interference of different harmonic contributions to the Volkov phase, i.e., due to the oscillating motion of the photoelectron in the laser pulse. Obviously, both ATI spectra coincide, as for all other laser parameters tested in our computations. This can be seen

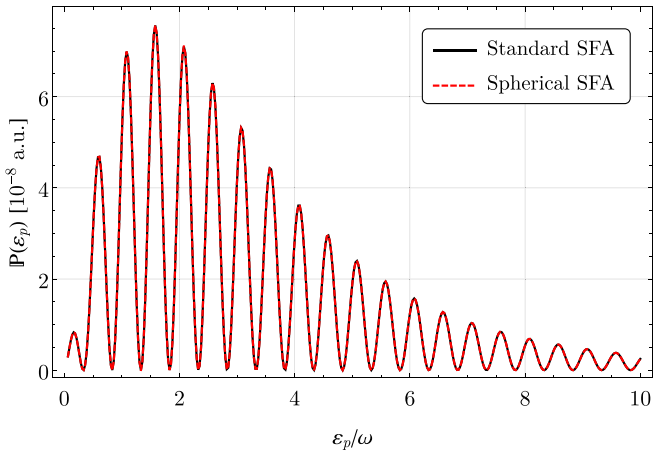

FIG. 2. ATI spectra computed within the standard SFA approach based on Eq. (4b), black solid lines, and the partial-wave expansion Eq. (23), red dashed lines, for photoelectrons emitted into the polar and azimuthal angles $\vartheta_p^{(0)} = \pi/2$ and $\varphi_p^{(0)} = 0$, respectively. The following parameters were used: hydrogen-like initial state with $n = 1$, $\ell = 0$, $m = 0$, $I_p = -\varepsilon_i = 14\,\text{eV}$ (krypton); plane-wave Volkov continuum states; and sine-squared laser pulse with $n_p = 2$, $\omega = 0.057$ a.u., $I_{\text{max}} = 5 \times 10^{13}$ W/cm^2, $\varepsilon = 1$ (circular polarization), $\lambda = +1$, $\phi_{\text{CEP}} = \pi$.

as verification that Eqs. (4b) and (23) are indeed (mathematically) equivalent. While the standard form of the SFA transition amplitude (4b) can be evaluated quite easily for the $1s$ initial state (of hydrogen-like ions) and for plane-wave Volkov states, it requires a considerable effort to perform analog computations for other initial and continuum states. In our partial-wave expansion (23), in contrast, no additional (analytical) work is needed, and this advantage may justify the slightly longer computation times mentioned above.

B. Dependence on the pulse shape

Modern experiments are able to produce different pulse shapes and often assume a Gaussian pulse envelope [36,37]. Moreover, several theoretical studies have demonstrated the dependence of strong-field (ionization) processes on the envelope of the driving laser pulse [23,24]. Despite these studies, however, it has been found convenient in SFA computations to assume laser pulses with a sine-squared envelope, mainly because this shape supports an analytical evaluation of the Volkov phase $S_V(t)$ and its exponential as it appears in the transition amplitude. The remaining time integration in the transition amplitude can then be solved either analytically (using the Jacobi-Anger expansion) or numerically. For Gaussian pulses, in contrast, such an analytical evaluation is not feasible owing to the error function that occurs in the Volkov phase [cf. Appendix B]. In the partial-wave expansion above, the time integrals only occur in the pulse-shape integrals (24) and are of course the same as in the standard formulation. For short pulses ($n_p \lesssim 20$ cycles), the pulse-shape integrals can be solved numerically with reasonable effort, while an analytically time integration might be favorable for long pulses. However, since the precise form of the pulse envelope becomes less relevant for the ATI spectra decreases with increasing pulse duration, a sine-squared pulse shape or a continuous beam is often a good first approximation.

Here we shall examine the influence of the pulse envelope $f(t)$ on the ATI spectra that results from the pulse-shape integrals (24) for short pulses. In particular, we consider a sine-squared, Gaussian pulse and rectangular pulse, for which an identical pulse duration $T_p = 2T$ and cycle length $T = 2\pi/\omega$ are assumed and for which Fig. 3(a) shows the instantaneous intensity $I(t) = A_0^2 f^2(t)\omega_0^2 c/8\pi$ for the various pulse envelopes. To make the ATI spectra comparable for these pulses, we have chosen the maximum intensity of each pulse so that their time-integrated intensities are identical.

Figure 3(b) displays the ATI spectra as obtained for these three pulses and by using the partial-wave expansion (23) of the SFA amplitude from above. In fact, the spectrum for the sine-squared pulse (black solid curve) is the same as shown in Fig. 2. One easily sees from this figure that the three spectra deviate considerably from each other and that the overall maximum in the ATI spectrum is shifted toward higher energies for both the Gaussian and rectangular pulses. This shift arises from the ponderomotive energy $U_p \sim I$ of the photoelectron, which is smaller for the lower (average) intensities of the Gaussian and rectangular pulses. Furthermore, the energy spacing of the ATI peaks clearly differs for all three pulse shapes due to the different spectral composition of these pulses. Since the oscillations of the photoelectron within the continuum are determined by the frequency spectrum of the vector potential and directly affect the Volkov phase, these frequencies become visible in the ATI peak structure. For a Gaussian envelope, in particular, the pulse duration is defined by its full width at half maximum. Thus, in contrast to the sine-squared and rectangular pulses, the Gaussian pulse is not confined to the temporal interval $[0, 2T]$, leading to an effectively broader frequency spectrum and to a smaller spacing between the ATI peaks.

To conclude this discussion, we have seen that the ATI spectra strongly depend on the envelope used for rather (short) driving laser pulses. This dependence also shows the advantage of our reformulation that allows a much simpler comparison of different pulse shapes. Apart from the numerical computation of the pulse shape integrals (24), the pulse shape can be easily replaced by inserting the analytical expression for the Volkov phase given in Appendix B. In practice, the computation of the pulse shape integrals is more elaborate for Gaussian than for rectangular and sine-squared pulses owing to the (complex) error functions in the Volkov phase.

C. Coulomb interactions in the continuum

The observed ATI spectra can be reproduced *qualitatively* within the SFA already with plane-wave Volkov continuum states since the ATI peaks arise due to the interaction between the (quasi)free photoelectron and the oscillating electric field of the ionizing laser pulse. The peak structure matches particularly well for high photoelectron energies. However, the ionization probabilities from such plane-wave Volkov states often deviate strongly from experiment in the low-energy region [38]. In addition, the experimentally observed symmetries of the PMDs usually cannot be explained in detail by using plane-wave Volkov states [39]. The theoretical

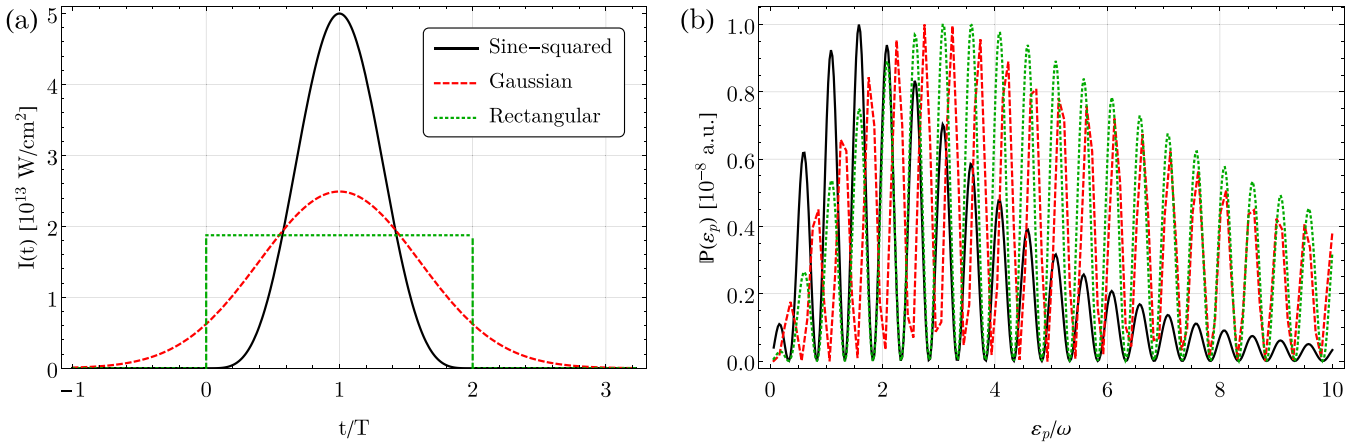

FIG. 3. Dependence of ATI spectra on the pulse shape. (a) Instantaneous laser intensity as a function of time for three different pulse envelopes $f(t)$ with identical pulse duration $T_p = n_p T$ where $n_p = 2$ and $T = 2\pi/\omega$; see Sec. III C. The respective maximum intensity was chosen such that the integral over the intensity is equal for all three pulse shapes (see main text). (b) ATI spectra computed for the pulse envelopes shown in panel (a) for photoelectrons emitted into the polar and azimuthal angles $\vartheta_p^{(0)} = \pi/2$ and $\varphi_p^{(0)} = 0$, respectively. All three spectra have been normalized to their respective maxima. The intensity was set to $I_{\max} = 5 \times 10^{13}$ W/cm^2 for the sine-squared pulse and all other parameters are the same as in Fig. 2. The labels in panel (a) also apply to the curves in panel (b).

predictions can be improved if the Coulomb potential of the residual ion is taken into account in the representation of the (Volkov) continuum [40,41]. This is readily done in the SFA by replacing the plane-wave Volkov continuum states by the Coulomb-Volkov states as discussed in Sec. III B 2. This replacement illustrates the role of the Coulomb interactions in the continuum [42], while further details in the ATI spectra and PMDs may require to deal also with the rescattering transition amplitude (4c), which is beyond the scope of this work [43].

For a Coulomb-Volkov continuum with the radial wave function (17) [instead of (13)], Fig. 4 displays the radial wave functions together with the ATI spectra for different values of the charge Z of the residual ion. The ATI spectra in Fig. 4(b) are shown on a logarithmic scale for the sake of better visibility. The black solid lines in Fig. 4 correspond to the plane-wave Volkov continuum or, equivalently, the Coulomb-Volkov continuum with $Z = 0$. The ATI spectra shown in Fig. 4(b) exhibit ATI peaks at identical values of the energy and independent of the ionic charge Z. In the SFA, this independence arises from the factorization of the Volkov phase factor in the Coulomb-Volkov states, which is therefore not influenced by the spatial part of the wave function. Nonetheless, it is easily seen that the ionization probability for $\varepsilon_p \lesssim 2\omega$ is enhanced by up to one order of magnitude if the ionic charge is continuously increased from $Z = 0$ to 1. While the photoelectron dynamics is solely driven by the laser field in the case of the plane-wave Volkov states, the attractive Coulomb potential of the residual ion pulls the electron toward the ion and reduces its kinetic energy [41]. Quantum

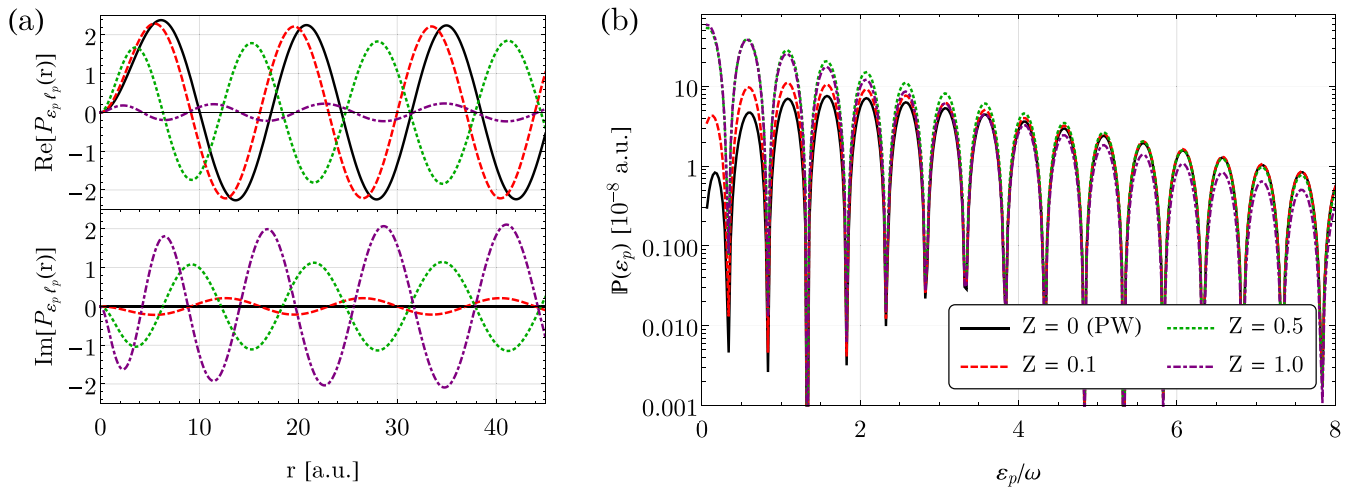

FIG. 4. Dependence of ATI spectra on the choice of the continuum states used in the SFA. (a) Real and imaginary parts of the radial wave function (17) of the Coulomb-Volkov states for $\varepsilon_p = 0.1$ a.u., $\ell_p = 1$ as well as for selected charge values $Z = 0$, 0.1, 0.5, 1.0 of the residual ion. (b) ATI spectra with Coulomb interactions in the continuum and for the same values of Z. These spectra were all computed from the transition amplitude (23) with the Coulomb-Volkov states (14) but otherwise the same parameters as in Fig. 2. The labels of residual charge are the same in both panels (a) and (b).

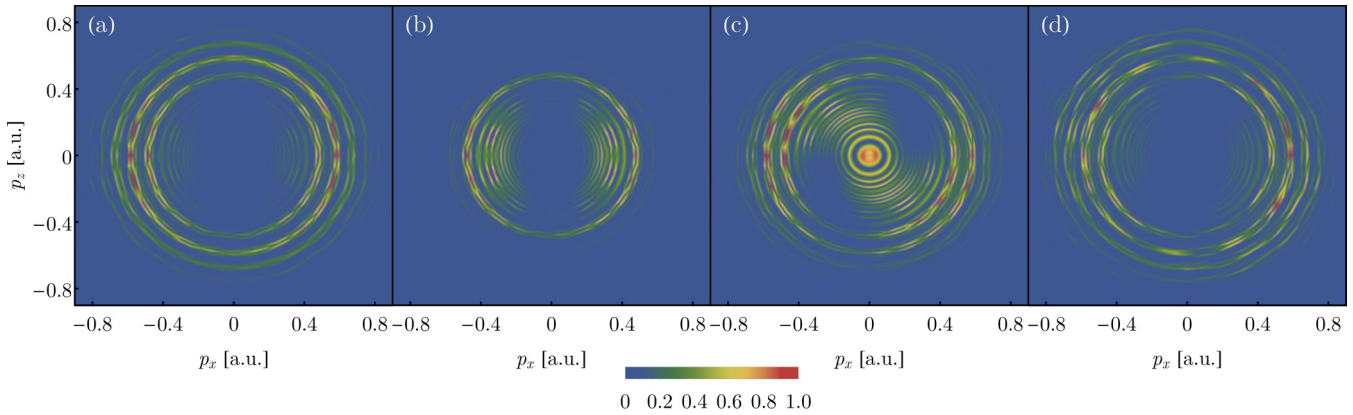

FIG. 5. PMDs $\mathbb{P}(p_x, p_y, p_z = 0)$ within the polarization plane of the driving laser pulse. Results are shown for a few selected (hydrogenic) initial states with $I_p = 14\,\text{eV}$ (krypton) and different representations of the photoelectron continuum: (a) hydrogen $1s$ wave function and plane-wave Volkov states, (b) hydrogen $4p$ ($m = +1$) wave function and plane-wave Volkov states, (c) hydrogen $4p$ ($m = +1$) wave function and Coulomb-Volkov states, and (d) hydrogen $4p$ ($m = +1$) wave function and atom-Volkov states. All these PMDs were normalized to their respective maximum. A sine-squared pulse with $n_p = 10$ and $I_{\text{max}} = 1.5 \times 10^{14}$ was used in the computations and all other parameters are the same as in Fig. 2.

mechanically, this can also be seen in the radial wave functions shown in Fig. 4(b), whose maxima are shifted toward smaller r if the ionic charge is increased. This attraction to the residual ion leads to the increased number of photoelectrons observed with low energy, i.e., the enhancement seen in Fig. 4(b).

The low-energy part of the ATI spectra can be further improved by adding a short-range potential to the (long-range) Coulomb potential and by using the Atom-Volkov states (see [19] and Sec. III B 3). We shall briefly discuss such a replacement and the influence of the initial bound state in the section below.

D. Dependence on the initial state

ATI experiments are often performed with noble gas targets and theoretical treatments can qualitatively reproduce the measured ATI spectra and PMDs under the assumption of a hydrogenic $1s$ initial state. Nevertheless, the SFA transition amplitude (4) depends on the specific model for the initial state and one can expect that more realistic initial states, adapted to the target atom that is ionized, lead to modified results. Indeed, this dependence was discussed in Refs. [21,22].

If PMDs are computed from the SFA transition amplitude (23) in the partial-wave expansion, the initial state, as given by Eq. (6), is defined via the quantum numbers n, ℓ and m, and its radial wave funtion $P_{n\ell}(r)$. No assumptions were made in our derivation in Sec. III regarding the precise model used for the initial state. In particular, its radial wave function, contained in the reduced matrix elements $\langle \varepsilon_p \ell_p \| \hat{\boldsymbol{p}} \| n\ell \rangle$, may either be assumed as hydrogenic or may be provided by a numerical scheme that accounts for the atomic structure.

Here, we briefly demonstrate the dependence of the PMDs on the choice of the initial state and limit our discussion to hydrogenic initial states for which the radial wave functions are analytically available (see, for example, Ref. [44]). For given principal quantum number n and ionization potential I_p, the effective nuclear charge is then determined via $Z = n\sqrt{2I_p}$. As in the previous sections, we consider a krypton target atom with $I_p = 14.0\,\text{eV}$. Figure 5 shows the PMDs in the polarization plane of the driving laser pulse as computed for a few selected initial states and different representations of the continuum. For a $1s$ initial state and plane-wave Volkov states (Sec. III B 1) in the continuum [Fig. 5(a)], the PMD clearly exhibits rings that correspond to the ATI peaks from above and have positions comparable to experimental findings [14]. The rings are visible only at large photoelectron momenta due to the rather high intensity and the linear color scale used for the photoionization probability. Furthermore, since a long ($n_p = 10$ cycles) circularly polarized laser pulse was assumed for which the vector potential is almost symmetric in the p_x-p_y plane, the angular distribution within every single ATI peak shows only a slight asymmetry [12].

In krypton, the active electron that is assumed to be ionized is a valence electron bound in a $4p$ state. In Fig. 5(b), we therefore show the PMD computed with a hydrogenic $4p$ initial state where we set the magnetic quantum number $m = +1$ and where the effective nuclear charge Z was adjusted so that I_p is identical to the $1s$ state above. As before, plane-wave Volkov continuum states are assumed. It can be observed that the rings in the PMD are shifted to smaller absolute values of the photoelectron momentum. This shift can be understood from the partial-wave expansion of the transition amplitude (23): The Clebsch-Gordan coefficients only allow transitions into continuum states with $\ell_p = \ell \pm 1$, reflecting angular momentum conservation. Therefore, for the $1s$ ($\ell = 0$) and $4p$ initial states ($\ell = 1$), different partial waves are populated in the ionization process. Since the corresponding radial wave functions (13) of the plane-wave Volkov states are farther removed from the origin in the latter case, the ionization probability decreases more rapidly with increasing p, leading to more pronounced peaks for small momenta in the normalized PMD.

In order to obtain even more realistic results, we may replace the continuum states in addition to the initial state, and in Fig. 5(c) we show the PMD computed for a $4p$ initial state and Coulomb-Volkov states (Sec. III B 2) in the continuum. As a result of the Coulomb interaction, the ionization probability for low photoelectron energies is enhanced as discussed

above and clearly discernible structures can be seen for low momenta in the PMD. Moreover, in comparison to Fig. 5(b), the rings in the outer part of the PMD are shifted toward larger absolute momenta. One can also observe that the angular distribution within the individual rings differs clearly from the PMDs in Figs. 5(a) and 5(b) and exhibits energy-dependent angular shifts of the maximum ionization probability. These angular shifts for circular polarization were discussed extensively in Refs. [45,46] as a result of the Coulomb interaction with the residual ion. However, it was found that in order to accurately reproduce these shifts, the *combined* interaction with Coulomb and laser fields needs to be accounted for, which is not included in the Coulomb-Volkov states.

One may try to further improve the results with an appropriate model for the ionic potential in the continuum. In Fig. 5(d), we therefore show the PMD computed with a $4p$ initial state and a continuum formed by atom-Volkov states (Sec. III B 3) that account for the combined Coulomb and short-range potentials of the residual Kr^+ ion, given by Eq. (18) with the parameters $a_1 - a_6$ taken from Ref. [32]. It can be seen that the low-energy structures of Fig. 5(c) have disappeared, since the short-range potential modifies the region of small radii around the ion and especially affects low-energy photoelectrons [41]. In addition, the rings have moved to larger absolute momenta compared to Fig. 5(c). Both the suppression of the ionization probability for small momenta and the shift of the maxima to higher energies have also been found in Ref. [19], in good agreement with the numerical solution of the time-dependent Schrödinger equation.

While the angular distributions within particular ATI peaks, i.e., on particular rings in the PMD, are different, we see that Figs. 5(a) and 5(d) are quite similar. Thus, in order to qualitatively reproduce the PMDs, a $1s$ initial state with a plane-wave Volkov continuum seems to be sufficient. For the computation of more precise PMDs, an initial state with the appropriate symmetry (here a p state) and atom-Volkov states should be used. The above results demonstrate the ability to easily compare different models for initial and continuum states within the partial-wave expansion of the SFA amplitude. It might be particularly interesting to replace the hydrogenic initial state with a numerical solution that accounts for the details of the target atom, obtained from numerical atomic-structure computations.

V. CONCLUSIONS

A reformulation of the SFA transition amplitude for a single active electron in terms of partial waves and spherical tensors has been presented for the ATI of atomic targets. In particular, the *direct* SFA transition amplitude was expressed in a modular form that allows for a simple replacement of the initial atomic bound state, the representation of the (Volkov) continuum, and the vector potential of the driving laser pulse. The resulting expansion (23) facilitates the comparison of different models. In addition, we discussed various representations of the photoelectron continuum and how the shape of the laser pulse affects the observed spectra and distribution.

We performed a series of test computations in order to verify the equivalence of the partial-wave expansion (23) in comparison with the standard SFA. Moreover, we demonstrated the dependence of the ATI spectra on the shape of the ionizing laser pulse as well as on the Coulomb interactions in the representation of the continuum. PMDs were computed especially for the ionization of krypton with hydrogen-like initial state wave functions for an active electron in the $1s$ and $4p$ shells. We also considered an atom-Volkov continuum that enables one to account for a short-range potential in addition to the (long-range) Coulomb potential of the photoion. These applications show how the expansion (23) helps to explore different approximations with regard to the initial bound state and the continuum.

In the future, one might examine several extensions of the SFA within the partial-wave formulation. In particular, the considerations of the present paper should be extended to account for the rescattering transition amplitude. In addition, the coupling to other atomic bound states might be included and relativistic or nondipole contributions to the dynamics can be incorporated. Furthermore, this expansion can be readily combined with atomic-structure computations (for example, Ref. [47]) to make further use of realistic matrix elements and amplitudes.

ACKNOWLEDGMENT

The work reported here was funded by the Deutsche Forschungsgemeinschaft (DFG, German Research Foundation), Grant No. 440556973.

APPENDIX A: EXPANSION OF COULOMB WAVES

The expansion (16) of the outgoing Coulomb waves (15) into spherical waves is given in terms of the function $w_{\ell_p}(\eta_p, pr)$ that were left unspecified in the main text. Their explicit form can be found if Eq. (16) is inserted into the Schrödinger equation with Hamiltonian $\hat{H} = \hat{\boldsymbol{p}}^2/2 + Z/r$, which transforms into a Whittaker equation for the w_{ℓ_p}. The solutions have the form [26]

$$w_{\ell_p}(\eta_p, pr) = \frac{1}{p} e^{i\sigma_{\ell_p}} F_{\ell_p}(\eta_p, pr),$$

with the so-called Coulomb phase shift

$$\sigma_{\ell_p} = \arg[\Gamma(\ell_p + 1 + i\eta_p)]$$

and the Coulomb function

$$F_{\ell_p}(\eta_p, pr) = \frac{2^{\ell_p}|\Gamma(\ell_p + 1 + i\eta_p)|}{(2\ell_p + 1)!} e^{-\pi\eta_p/2} (pr)^{\ell_p+1} e^{ipr} \times {}_1F_1(\ell_p + 1 + i\eta_p; 2\ell_p + 2; -2ipr).$$

In these equations, $\Gamma(x)$ is the Γ function and ${}_1F_1(a; b; z)$ is the confluent hypergeometric function [30].

APPENDIX B: VOLKOV PHASE FOR DIFFERENT PULSE SHAPES

In this Appendix, we briefly state the analytical expressions for the Volkov phase (11) for the different laser pulse shapes mentioned at the end of Sec. III C. We limit ourselves to circular polarization ($\varepsilon = 1$). Using the analytical expressions for the Volkov phase, the t integrals in the pulse shape integrals (24) occurring in the SFA transition amplitude can then be computed numerically.

In general, if the vector potential is given by Eqs. (20) and (21), the Volkov phase (11) can be evaluated to give

$$S_V(t) = \varepsilon_p t + \frac{A_0\, p\, \sin\vartheta_p}{\sqrt{2}} \int^t d\tau\; f(\tau)\cos(\omega\tau + \xi) + \frac{A_0^2}{4}\int^t d\tau\; f^2(\tau), \tag{B1}$$

where we defined $\xi = \phi_{\rm CEP} - \lambda\varphi_p$. This expression only depends on the pulse envelope $f(\tau)$ and the integrals can be solved analytically with the following results.

For a continuous laser beam [$f(t) \equiv 1$], we find

$$S_V(t) = (\varepsilon_p + U_p)t + a\sin(\omega t + \xi),$$

where $a = A_0 p \sin\vartheta_p/\sqrt{2}\omega$ and $U_p = A_0^2/4$ is the ponderomotive energy.

For a rectangular pulse [$f(t) = 1$ for $0 \leqslant t \leqslant T_p$; $f(t) = 0$ otherwise], Eq. (B1) yields

$$S_V(t) = \begin{cases} \varepsilon_p t, & t < 0 \\ (\varepsilon_p + U_p)t + a[\sin(\omega t + \xi) - \sin\xi], & 0 \leqslant t \leqslant T_p \\ \varepsilon_p t + U_p T_p + a[\sin(\omega T_p + \xi) - \sin\xi], & t \geqslant T_p \end{cases}.$$

Similarly, for a sine-squared pulse [$f(t) = \sin^2(\omega t/2n_p)$ for $0 \leqslant t \leqslant T_p$; $f(t) = 0$ otherwise], the Volkov phase is

$$S_V(t) = \begin{cases} \varepsilon_p t, & t < 0 \\ \varepsilon_p t + \frac{3}{8}U_p t - \frac{U_p n_p}{2\omega}\sin\left(\frac{\omega}{n_p}t\right) + \frac{U_p n_p}{16\omega}\sin\left(2\frac{\omega}{n_p}t\right) & \\ +a\sum_{k=-1}^{1}\frac{c_k}{1+\frac{k}{n_p}}\left[\sin\left(\omega\left(1+\frac{k}{n_p}\right)t + \xi\right) - \sin\xi\right], & 0 \leqslant t \leqslant T_p \\ \varepsilon_p t + \frac{3}{8}U_p T_p - \frac{U_p n_p}{2\omega}\sin\left(\frac{\omega}{n_p}T_p\right) + \frac{U_p n_p}{16\omega}\sin\left(2\frac{\omega}{n_p}T_p\right) & \\ +a\sum_{k=-1}^{1}\frac{c_k}{1+\frac{k}{n_p}}\left[\sin\left(\omega(1+\frac{k}{n_p})T_p + \xi\right) - \sin\xi\right], & t \geqslant T_p \end{cases},$$

where $c_\pm = -1/4$ and $c_0 = 1/2$.

For a Gaussian pulse [$f(t) = e^{-4\ln(2)(t/T_p)^2}$], we find from Eq. (B1)

$$\begin{aligned} S_V(t) = {} & \varepsilon_p t + U_p\sqrt{\frac{\pi}{\ln(4)}}\frac{T_p}{4}\,\mathrm{erf}\left(2\sqrt{\ln(4)}\frac{t}{T_p}\right) \\ & + \frac{A_0\, p\, \sin\vartheta_p}{\sqrt{2}}\frac{T_p}{8}\sqrt{\frac{\pi}{\ln(2)}}\,e^{-\frac{\omega^2 T_p^2}{\ln(65536)}}\left[e^{-i\xi}\,\mathrm{erf}\left(\frac{iT_p^2\omega + 8\ln(2)t}{4T_p\sqrt{\ln(2)}}\right) - e^{i\xi}\,\mathrm{erf}\left(\frac{iT_p^2\omega - 8\ln(2)t}{4T_p\sqrt{\ln(2)}}\right)\right], \end{aligned}$$

where $\mathrm{erf}(x)$ is the error function [30].

APPENDIX C: REDUCED MATRIX ELEMENTS OF $\hat{\boldsymbol{p}}$

In this Appendix, we explicitly evaluate the reduced matrix elements of the momentum operator $\hat{\boldsymbol{p}}$ that appear in the transition amplitude (23). To this end, we start from the initial state (6) and the general form of the continuum states defined by Eqs. (7) and (8).

The momentum operator can be expressed as a tensor operator of rank 1 in the form [26]

$$\hat{\boldsymbol{p}} = -i\boldsymbol{\nabla} = -i\left[\boldsymbol{C}^1\frac{\partial}{\partial r} - \frac{\sqrt{2}}{r}(\boldsymbol{C}^1 \times \boldsymbol{L})^1\right],$$

where $\boldsymbol{C}^1$ is the tensor operator constructed from spherical harmonics with components

$$C_{1q}(\vartheta, \varphi) = \left(\frac{4\pi}{3}\right)^{1/2} Y_{1q}(\vartheta, \varphi).$$

Therefore, the reduced matrix element of $\hat{\boldsymbol{p}}$ can also be written as

$$\langle\varepsilon_p \ell_p \|\hat{\boldsymbol{p}}\| n\ell\rangle = -i\,\langle\ell_p\|\boldsymbol{C}^1\|\ell\rangle\,\langle\varepsilon_p|\hat{\mathcal{D}}_r|n\rangle$$

with the operator

$$\hat{\mathcal{D}}_r = \frac{\partial}{\partial r} - \frac{(\ell_p - \ell)(\ell_p + \ell + 1) - 2}{2r},$$

and the reduced matrix elements of the spherical harmonics tensor

$$\langle\ell_p\|\boldsymbol{C}^1\|\ell\rangle = -\sqrt{2\ell_p + 1}\,\langle\ell_p\, 0,\, 1\, 0|\ell\, 0\rangle\,.$$

With these identities, the reduced matrix elements of $\hat{\boldsymbol{p}}$ are given by

$$\langle \varepsilon_p \ell_p \| \hat{\boldsymbol{p}} \| n\ell \rangle = (-i)^{\ell_p+1} \, \langle \ell_p \| \boldsymbol{C}^1 \| \ell \rangle \int_0^\infty dr \, \frac{P^*_{\varepsilon_p \ell_p}(r)}{r} \left[r \frac{\partial P_{n\ell}(r)}{\partial r} - \frac{(\ell_p - \ell)(\ell_p + \ell + 1)}{2} \, P_{n\ell}(r) \right]. \tag{C1}$$

This result is valid for any description of the one-electron continuum and can be evaluated using the explicit form of the radial wave functions, i.e., Eq. (13) for plane-wave Volkov states, Eq. (17) for Coulomb-Volkov states, and Eq. (19) for atom-Volkov states.

[1] P. Agostini, F. Fabre, G. Mainfray, G. Petite, and N. K. Rahman, Phys. Rev. Lett. **42**, 1127 (1979).

[2] G. G. Paulus, W. Nicklich, H. Xu, P. Lambropoulos, and H. Walther, Phys. Rev. Lett. **72**, 2851 (1994).

[3] A. McPherson, G. Gibson, H. Jara, U. Johann, T. S. Luk, I. A. McIntyre, K. Boyer, and C. K. Rhodes, J. Opt. Soc. Am. B **4**, 595 (1987).

[4] M. Ferray, A. L'Huillier, X. F. Li, L. A. Lompre, G. Mainfray, and C. Manus, J. Phys. B: At. Mol. Opt. Phys. **21**, L31 (1988).

[5] B. Walker, B. Sheehy, L. F. DiMauro, P. Agostini, K. J. Schafer, and K. C. Kulander, Phys. Rev. Lett. **73**, 1227 (1994).

[6] K. C. Kulander, Phys. Rev. A **38**, 778 (1988).

[7] L. V. Keldysh, Sov. Phys. JETP **20**, 1307 (1965).

[8] F. H. M. Faisal, J. Phys. B: At. Mol. Phys. **6**, L89 (1973).

[9] H. R. Reiss, Phys. Rev. A **22**, 1786 (1980).

[10] S. V. Popruzhenko, J. Phys. B: At. Mol. Opt. Phys. **47**, 204001 (2014).

[11] K. Amini, J. Biegert, F. Calegari, A. Chacón, M. F. Ciappina, A. Dauphin, D. K. Efimov, C. F. de Morisson Faria, K. Giergiel, P. Gniewek, A. S. Landsman, M. Lesiuk, M. Mandrysz, A. S. Maxwell, R. Moszyński, L. Ortmann, J. A. Pérez-Hernández, A. Picón, E. Pisanty, J. Prauzner-Bechcicki, K. Sacha, N. Suárez, A. Zaïr, J. Zakrzewski, and M. Lewenstein, Rep. Prog. Phys. **82**, 116001 (2019).

[12] D. B. Milošević, G. G. Paulus, D. Bauer, and W. Becker, J. Phys. B: At. Mol. Opt. Phys. **39**, R203 (2006).

[13] J. H. Bauer and Z. Walczak, Phys. Rev. A **101**, 063409 (2020).

[14] T. J. McIlrath, P. H. Bucksbaum, R. R. Freeman, and M. Bashkansky, Phys. Rev. A **35**, 4611 (1987).

[15] S. Basile, F. Trombetta, G. Ferrante, R. Burlon, and C. Leone, Phys. Rev. A **37**, 1050 (1988).

[16] F. Trombetta, S. Basile, and G. Ferrante, J. Opt. Soc. Am. B **6**, 554 (1989).

[17] D. G. Arbó, J. E. Miraglia, M. S. Gravielle, K. Schiessl, E. Persson, and J. Burgdörfer, Phys. Rev. A **77**, 013401 (2008).

[18] F. H. M. Faisal, Phys. Rev. A **94**, 031401(R) (2016).

[19] D. B. Milošević and W. Becker, Phys. Rev. A **99**, 043411 (2019).

[20] A. Sanpera, J. B. Watson, M. Lewenstein, and K. Burnett, Phys. Rev. A **54**, 4320 (1996).

[21] J. H. Bauer, J. Phys. B: At. Mol. Opt. Phys. **41**, 185003 (2008).

[22] J. H. Bauer, J. Phys. B: At. Mol. Opt. Phys. **46**, 045601 (2013).

[23] M. Ciappina, J. Pérez-Hernández, and M. Lewenstein, Comput. Phys. Commun. **185**, 398 (2014).

[24] R. Della Picca, A. A. Gramajo, C. R. Garibotti, S. D. López, and D. G. Arbó, Phys. Rev. A **93**, 023419 (2016).

[25] W. J. Thompson, *Angular Momentum: An Illustrated Guide to Rotational Symmetries for Physical Systems*, 1st ed. (John Wiley and Sons, New York, 2008).

[26] I. P. Grant, *Relativistic Quantum Theory of Atoms and Molecules*, 1st ed. (Springer, New York, 2007).

[27] R. H. Landau, *Quantum Mechanics II*, 2nd ed. (Wiley-VCH, Weinheim, 2004).

[28] D. Bauer, D. B. Milošević, and W. Becker, Phys. Rev. A **72**, 023415 (2005).

[29] M. Jain and N. Tzoar, Phys. Rev. A **18**, 538 (1978).

[30] M. Abramowitz and I. Stegun (eds.), *Handbook of Mathematical Functions with Formulas, Graphs, and Mathematical Tables*, 10th ed. (U.S. Department of Commerce, National Bureau of Standards, Washington, DC, 1972).

[31] X. M. Tong and C. D. Lin, J. Phys. B: At. Mol. Opt. Phys. **38**, 2593 (2005).

[32] D. B. Milošević, W. Becker, M. Okunishi, G. Prümper, K. Shimada, and K. Ueda, J. Phys. B: At. Mol. Opt. Phys. **43**, 015401 (2009).

[33] A. Čerkić, E. Hasović, D. B. Milošević, and W. Becker, Phys. Rev. A **79**, 033413 (2009).

[34] D. A. Varshalovich, A. N. Moskalev, and V. K. Khersonskii, *Quantum Theory of Angular Momentum* (World Scientific, Singapore, 1988).

[35] B. Böning, W. Paufler, and S. Fritzsche, Phys. Rev. A **99**, 053404 (2019).

[36] M. Wollenhaupt, T. Bayer, and T. Baumert, in *Ultrafast Dynamics Driven by Intense Light Pulses: From Atoms to Solids, from Lasers to Intense X-rays*, edited by M. Kitzler and S. Gräfe (Springer International, Cham, 2016), pp. 63–122.

[37] C. D. Lin, A.-T. Le, C. Jin, and H. Wei, *Attosecond and Strong-Field Physics: Principles and Applications* (Cambridge University Press, Cambridge, UK, 2018).

[38] C. I. Blaga, F. Catoire, P. Colosimo, G. G. Paulus, H. G. Muller, P. Agostini, and L. F. DiMauro, Nat. Phys. **5**, 335 (2009).

[39] S. P. Goreslavski, G. G. Paulus, S. V. Popruzhenko, and N. I. Shvetsov-Shilovski, Phys. Rev. Lett. **93**, 233002 (2004).

[40] W. Quan, Z. Lin, M. Wu, H. Kang, H. Liu, X. Liu, J. Chen, J. Liu, X. T. He, S. G. Chen, H. Xiong, L. Guo, H. Xu, Y. Fu, Y. Cheng, and Z. Z. Xu, Phys. Rev. Lett. **103**, 093001 (2009).

[41] C. Y. Wu, Y. D. Yang, Y. Q. Liu, Q. H. Gong, M. Y. Wu, X. Liu, X. L. Hao, W. D. Li, X. T. He, and J. Chen, Phys. Rev. Lett. **109**, 043001 (2012).

[42] J. Zhang and T. Nakajima, Phys. Rev. A **75**, 043403 (2007).
[43] F. H. M. Faisal and S. Förster, J. Phys. B: At. Mol. Opt. Phys. **51**, 234001 (2018).
[44] B. H. Bransden and C. J. Joachain, *Physics of Atoms and Molecules* (Prentice Hall, Harlow, 2003).
[45] C. P. J. Martiny, M. Abu-samha, and L. B. Madsen, J. Phys. B: At. Mol. Opt. Phys. **42**, 161001 (2009).
[46] M.-H. Yuan and X.-B. Bian, Phys. Rev. A **101**, 013412 (2020).
[47] S. Fritzsche, Comput. Phys. Commun. **240**, 1 (2019).